Core-Levels, Band Alignments and Valence Band States in $CuSbS_2$

Thomas J. Whittles[a], Tim D. Veal[a], Christopher N. Savory[b], Adam W. Welch[c], Francisco Willian de Souza Lucas[c], James T. Gibbon[a], Max Birkett[a], Richard J. Potter[d], David O. Scanlon[b], Andriy Zakutayev[c], Vin R. Dhanak[a]

[a]Stephenson Institute for Renewable Energy and Department of Physics, University of Liverpool, Liverpool L69 7ZF, United Kingdom

[b]University College London, Department of Chemistry, Christopher Ingold Building, London WC1H 0AJ, United Kingdom

[c]National Renewable Energy Laboratory, material Science Center, 15013 Denver W Parkway, Golden, CO 80401, USA

[d]Centre for Materials and Structures, School of Engineering, University of Liverpool, Liverpool L69 3GH, United Kingdom

Abstract

The earth-abundant material $CuSbS_2$ (CAS) has been demonstrated to have good optical properties as a photovoltaic solar absorber material, but to date it has seen relatively poor solar cell performance. Here, x-ray photoemission spectroscopy (XPS) is used to probe the core-levels of the constituent elements and surface contaminants and also to measure the ionisation potential and valence band spectra. The ionisation potential and electron affinity for this material (4.98 eV/3.43 eV) are lower than for other common absorbers, including $CuIn_xGa_{(1-x)}Se_2$ (CIGS). By comparing the valence band spectra from XPS and density functional theory (DFT), the VBM is shown to be raised due to the lone pair electrons from the antimony cations contributing additional state when compared with indium or gallium cations in CIGS. The resulting conduction band misalignment with CdS is a reason for the poor performance of cells incorporating a CAS/CdS heterojunction, supporting the idea that using a cell design analogous to CIGS is unhelpful. Thus, with a greater knowledge of the underlying electronic structure, cell architectures can be redesigned.

Introduction

The drive to discover and develop materials for use in terawatt-scale thin film photovoltaics (PV) has grown somewhat in recent years, due to the necessity of eliminating environmentally harmful or economically unfeasible elemental components from their production, as is the case with the current market leaders, cadmium telluride (CdTe) or copper indium gallium diselenide (CIGS)[1–4]. One attractive family of materials for this purpose is the ternary copper chalcogenides, taking the general form $Cu_mM_nCh_x$ (M = Sb, Bi; Ch = S, Se), developed as an analogue to CIGS, replacing trivalent In and Ga with Sb or Bi[1,5,6].

Here, the compound $CuSbS_2$ (CAS) is of interest, which has previously demonstrated appealing photovoltaic properties[7,8]. With scarcity and world demand for antimony being significantly lower than for indium[6], as well as having almost equivalent ionic radii[9], this metal could prove a good substitute, both economically and in terms of PV properties. Long known as the naturally occurring mineral chalcostibite[10], it was not realised as a solar absorber until 2001[5], with the first cell being constructed in 2005[11], and has since demonstrated a solar-matched band gap of ~1.5 eV[5,12,13], inherent p-type conductivity due to the dominant copper vacancy[5,14,15], and absorption stronger than both CIGS and another popular earth-abundant absorber, copper zinc tin sulphide (CZTS)[7]. CAS has a relatively low melting point of ~540°C[2,15], and so is amenable to crystallisation at lower temperatures. CAS has

thus far been successfully grown in thin film and nanoscale form by many and varied deposition methods, both physical (thermal evaporation[2,16–18] and sputtering[3,4,19]) and chemical (spray pyrolysis[14,20,21], chemical bath[5,11,12,22], spin coating[15], electrodeposition[13,16,23], solution processing[24] and solvo-/hydro-thermal[25–27]), leading to continued interest in the material. Beyond its use as a solar absorber, interest is also maintained in CAS because of its potential use in other areas of semiconductor applications, such as supercapacitors[28], dye-sensitised solar cells[29,30], or electrodes in batteries[31].

Despite this, solar cell performance thus far has been severely limited and the shortcomings of the literature reports on device properties have been previously ackowledged[3]. There have been very few reports of fully built PV devices and those that do exist commonly report no[9,11,22], or very low (<2%)[2,4,15,17] efficiencies. The efficiency record currently stands at only 3.22%[32], with another study reporting a near-record efficiency of 3.13%[13] and even after over a decade of research, recent reports still acknowledge that further investigation into device fabrication and characterisation is required[7,17].

Although antimony takes the trivalent oxidation state in CAS, like Ga/In does in CIGS, CAS does not form in the tetrahedral chalcopyrite crystal structure like CIGS[33,34]. Instead, CAS forms in a structure (shown in Figure 1) that is somewhat distorted by the stereochemically active antimony lone pair electrons, which do not take part in bonding[35]. The copper atoms are 4-fold coordinated to sulphur in almost regular tetrahedra, whereas the antimony atoms are 5-fold coordinated to sulphur in a distorted square-based pyramid arrangement. The lone pair electron density is then directed into the void between the SbS_5 pyramid units[36]. With two Sb-S bonds being much longer than the other three[37] (shown as grey in Figure 1), the crystal structure is said to be layered through the plane intersecting these bonds[4]. Consequently, there are two inequivalent sulphur sites, one which is coordinated to two Cu and three Sb atoms, and the other which is coordinated to two Cu and two Sb atoms[1] (labelled S1 and S2 in Figure 1, respectively). This structure, which is very dissimilar from that of CIGS or CZTS[3], leads to some differing characteristics, thought to be the cause of the poor device performances. It is the details of the electronic structure of CAS which are explored in the present study.

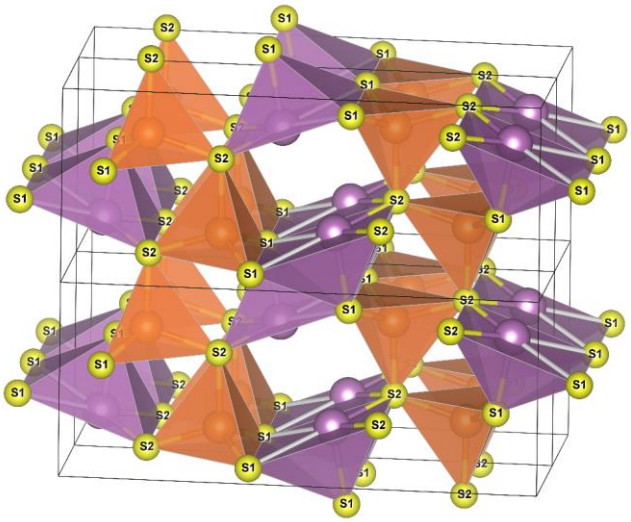

Figure 1: Crystal structure of chalcostibite[37] $CuSbS_2$, showing the individual atoms of Cu (orange), Sb (purple) and S (yellow). The inequivalent sulphur coordination sites are marked.

In this article, we present a full x-ray photoemission spectroscopy (XPS) analysis of $CuSbS_2$, including core-levels, the effect of surface cleaning and contamination, along with valence band spectra and the position of the band edges. From this, we show how complexities in the spectra can make the surface

contamination of this material easy to overlook, and how it is important to identify and recognise the effects of such surface contamination. We then corroborate the findings within the valence band with theoretical density of states calculations in order to further explain the bonding nature of this material and how this affects the position of the VBM. This then gives rise to a low ionisation potential, which is partly responsible for the poor efficiencies seen so far because of the poor conduction band alignment with the commonly used window layer, CdS.

Experimental Methods

The films of phase-pure polycrystalline $CuSbS_2$ (~1.5 µm thickness) were synthesised by co-sputtering from Sb_2S_3 and Cu_2S targets on bare and Mo-coated soda lime glass substrates heated to 350°C. To improve the quality of the $CuSbS_2$ material, some of the resulting thin film samples were annealed at 450− 500°C for 11 hours in a tube furnace under flow of N_2 in the presence of sacrificial Sb_2S_3 powder. The results for the annealed $CuSbS_2$ thin films are presented below, whereas the results of as-deposited $CuSbS_2$ thin films are provided in the SI. More details about the synthesis[19] and annealing[3] of the $CuSbS_2$ thin films have been previously reported.

Raman spectra were acquired using a Horiba Scientific Jobin-Yvon LabRam HR system. This consisted of a confocal microscope coupled to a single grating spectrometer, equipped with a notch filter and a CCD camera detector. Spectra were measured using an incident wavelength of 514.5 nm from an argon ion laser in backscattering geometry with an exposure time of 30 s and 5 acquisitions, over a range of 100-1500 cm^{-1}. Before measurements, the spectrometer was calibrated to the laser wavelength and the Si 520cm^{-1} mode.

Optical transmission and specular reflection spectra were recorded at 4 and 300 K and for photon energies of 0.3 to 2.4 eV at an angle of incidence of 11° to the surface normal using a combined reflection transmission accessory in a Bruker Vertex 70v Fourier-transform infrared (FTIR) spectrometer. The low temperature was obtained using an Oxford Instruments CFV2 continuous-flow helium cryostat. The vacuum pressures were 2 mbar for the optical path in the spectrometer and 1×10^{-6} mbar in the sample environment of the cryostat. The procedure for reduction of the transmission and reflection spectra to obtain absorption spectra is described elsewhere[38].

XPS measurements were performed in a standard ultrahigh vacuum (UHV) chamber operating at a base pressure of less than 2×10^{-10} mbar with hydrogen as the main residual gas. Samples were attached to the sample plates by spot welding tantalum straps across the sample edges. This also provided an electrical connection between the CAS films and the spectrometer. In vacuo sample cleaning was performed by means of Ar^+ ion sputtering and a radiative heating stage. The core-level electronic structure, valence band density of states and secondary electron cutoff (SEC) were measured using monochromated Al Kα X-ray radiation, operating nominally at 250 W, details of which, including the calibration of the spectrometer, are described elsewhere[39].

Samples were sputtered and annealed in order to remove surface contaminants including oxides and hydrocarbons which inevitably form due to handling in ambient atmosphere. During cleaning, the samples were monitored by XPS and were considered to be clean when the C 1s peak and peaks due to antimony oxide were no longer visible on the survey spectra. Such cleanliness was achieved by grazing angle (20°) sputtering with 500 eV Ar^+ in 5 minute steps (30 minutes total) followed by annealing at 200°C for 60 minutes. Relatively low energy and a grazing angle of incidence were used in order to minimise sample damage. This cleaning facilitated the measurement of a more representative surface of $CuSbS_2$ and hence, prevented the valence band (VB) spectra from being overwhelmed by signal from the contamination. It is noted however, that a full set of XPS spectra was

taken prior to surface cleaning to demonstrate the changes taking place and also the tendency of oxide formation at the surface of this material.

Prior to cleaning, the main C 1s signal, due to contaminant carbon, was found to have a binding energy (BE) of 284.7 eV and was deemed to have either experienced no, or very minimal charging due to this binding energy being observed for contaminant carbon on this material previously.[2,9,22,40,41] However, after subjecting the sample to surface cleaning, the very poor signal to noise ratio for the C 1s peaks meant that this peak could no longer be used for charge correction. Instead, it is believed the copper in the sample should be affected least by cleaning, and as such, the copper $2p_{3/2}$ peak should demonstrate the same BE throughout. Therefore, the spectra were calibrated using the Cu $2p_{3/2}$ BE of the sample prior to cleaning, which was measured to be 932.0 eV.

Computational Modelling

All periodic Density Functional Theory (DFT) calculations in this article were performed through the Vienna Ab Initio Simulation Package (VASP)[42–45]. The screened hybrid functional HSE06[46] was used for geometry optimization and the density of states calculations. HSE06 includes 25% Hartree-Fock exchange, which is screened with a parameter of w = 0.11 $bohr^{-1}$, with 75% exchange and full correlation from the Generalized Gradient Approximation (GGA) functional PBE[47]. This method has been used successfully in previous reports on $CuSbS_2$ and other antimony sulfides[1,7,48]. The projector-augmented wave method was used to describe the interaction between valence and core electrons, and scalar-relativistic pseudopotentials were used[49]. A cut-off energy of 375 eV and a Γ-centred k-point mesh of 4 × 7 × 2 were used in all calculations, determined to be sufficient to converge the total energy to within 1 meV/atom. A convergence criterion of 0.01 eV $Å^{-1}$ on the forces per atom was used for the geometry optimization, and the cut-off energy was increased to prevent errors arising from Pulay stress.

Results and Discussion

The Raman spectrum for the $CuSbS_2$ sample is shown in Figure 2 and demonstrates a single intense peak at 355 cm^{-1}, which is indicative of the chalcostibite phase[50]. Also observed are the weaker Raman modes at 101, 140 and 164 cm^{-1} which have been reported previously for this material[2]. The Raman modes corresponding to Sb_2S_3[51], CuS[52,53] and the other stoichiometries of copper antimony sulphide, Cu_3SbS_3[54], Cu_3SbS_4[55] and $Cu_{12}Sb_4S_{13}$[50], are not present in the spectrum. This, and previous x-ray diffraction (XRD) measurements of samples prepared using an identical method[3], suggest that the $CuSbS_2$ is phase-pure.

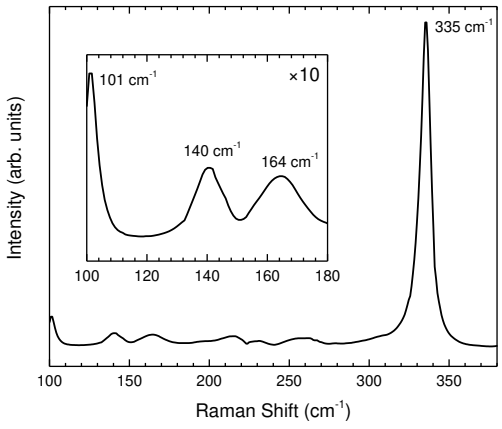

Figure 2: Raman spectrum for the $CuSbS_2$ sample.

Core-Level XPS

XPS can be used as a powerful tool in determining the oxidation states present in a grown material and is often used in conjunction with XRD. In addition, it can also be used to identify and determine the effects of surface contamination of materials, which could cause detriment to device performance. Unfortunately, complexities in the spectra can lead to misinterpretations, and a discussion of these with regards to CAS is given in the SI, which led to the adoption of the fitting procedure applied below.

The survey spectra for the sample, both before and after surface cleaning, are shown in Figure 3, and demonstrate peaks for the expected elements of copper, antimony and sulphur from the material. Peaks from carbon and oxygen are also present; not unexpected because of hydrocarbon contamination from exposure to atmosphere, which then subsequently reduced after cleaning. Sodium was also found, which did not decrease on cleaning, suggesting that the sodium has diffused through from the glass, as has been seen in similar materials[56]. Further discussion of the nature and effects of sodium with the corresponding spectra can be found in the SI.

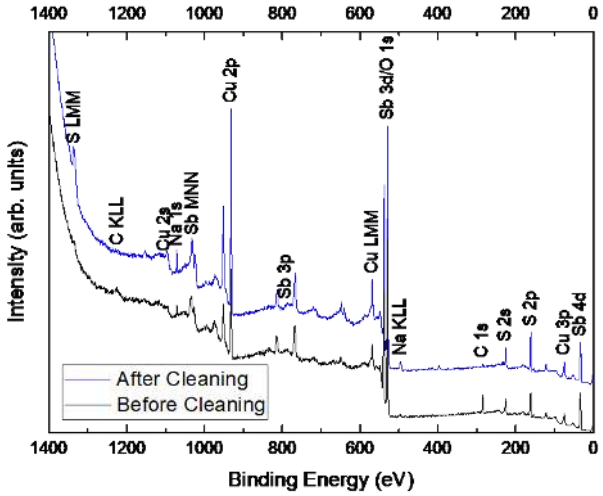

Figure 3: XPS survey spectra for the CAS sample before and after surface cleaning.

The following is an analysis of the high resolution spectra for the regions of interest in this material, and a summary of the fitted binding energies and FWHM of the core-levels described below is given in Table 1. All spectra were fitted using Voigt functions after a Shirley background had been subtracted. Further details of the analysis, with the associated spectra, and values for surface stoichiometry can be found in the SI.

The Cu 2p spectra were fitted with one doublet separated by 19.8 eV[57] and with an area ratio of 1:2, attributed to Cu^{+} in $CuSbS_2$. The FWHM of the Cu $2p_{1/2}$ peak is somewhat broader than that of the Cu $2p_{3/2}$ peak due to Coster-Kronig effects[58,59]. Because charge correction was achieved using the Cu $2p_{3/2}$ peak, all spectra are nominally similar, and a comparison before and after cleaning is shown in Figure 4. It can be seen that no discernible change occurred during the cleaning process, showing no oxidation of the copper in the material after growth and demonstrating the quality of the samples, as previous samples had revealed oxidation of the copper[26].

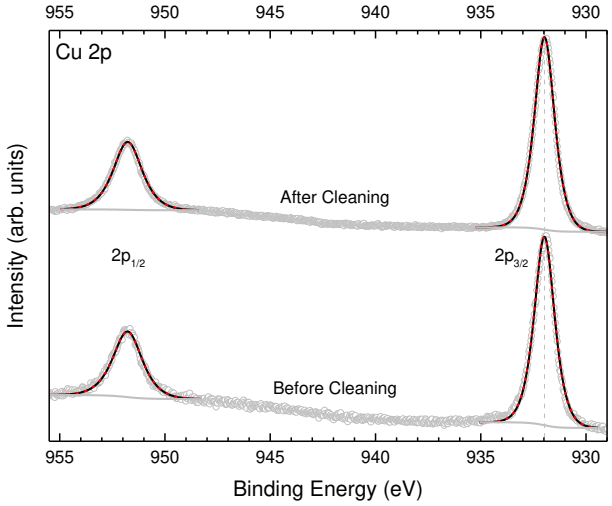

Figure 4: XPS spectra for the Cu 2p region of the CAS sample before and after surface cleaning. Fitted peaks shown in red and peak envelope shown in black.

The overlapping regions of Sb 3d and O 1s were fitted according to the procedure detailed in the SI, and the spectra before and after cleaning are shown in Figure 5. It can be seen that prior to cleaning, two distinct peaks are visible in the Sb $3d_{3/2}$ region, with a shoulder to the lower binding energy side of the lower peak (~537 eV). These features were fitted with three Sb 3d doublets, and the remaining intensity in the Sb $3d_{5/2}$ region, relating to O 1s emission, was fitted with two peaks. The strongest, sharpest antimony doublet (red dash) was attributed to Sb^{3+} in $CuSbS_2$, sharpest because of the high crystallinity of the intentionally grown material. The doublet at highest binding energy (pink dot) was attributed to antimony in a Sb-O environment. It is thought that this oxide consists predominantly of Sb_2O_3, as the trivalency of antimony is maintained and the binding energy is in agreement with literature values[60], however it is possible that the oxide is a mixture of Sb_2O_3 and Sb_2O_5 because the literature is unclear on the distinction between the two oxides in the spectra[61–64]. Nevertheless, this Sb-O species is drastically reduced on surface cleaning, showing that the oxide is present only at the surface of the sample and formed during atmospheric exposure. After cleaning, a small amount of oxide remained on the surface, which was not removed to avoid inducing sample damage through prolonged, excessive sputtering. It is also possible that this remnant oxide is present in the bulk of the sample and so could not be removed by surface cleaning, however due to the low level of oxide remaining (see SI for details), it is thought to have little effect on the measurements. The O 1s peak at higher binding energy (orange shading) is consistent with an adventitious species associated with carbon[65] and the peak at lower binding energy (purple shading), almost fully overlapping the antimony oxide Sb $3d_{5/2}$ peak, is attributed to the oxygen from within this antimony oxide[62], which subsequently reduced upon cleaning as well. The third, small antimony doublet (blue dot dash), present at lower binding energy is attributed to metallic antimony[61]. It is believed that the metallic antimony is not created by the preferential sputtering of sulphur, nor the dissociation of sulphur during the surface cleaning for several reasons. Firstly, the amount of metallic antimony relative to the antimony from CAS decreases after surface cleaning, whereas if it were created by the surface cleaning, one would expect it to increase. Secondly, surface cleaning-induced damage to the sample was minimised by using relatively low sputtering energies and anneal temperatures, as detailed in the experimental section, because in a study where high energy sputtering was used (3 keV)[9,22], the amount of sputter-induced antimony was markedly higher and could have a significant effect on the measurements.

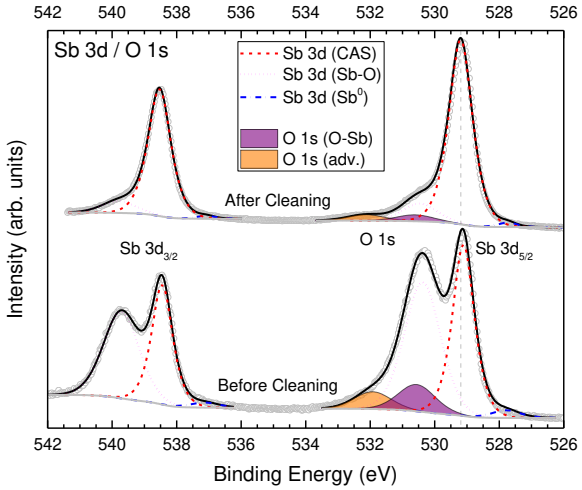

Figure 5: XPS spectra for the Sb 3d and O 1s overlap region of the CAS sample before and after surface cleaning. Peak envelope shown in black.

A comparison of the S 2p spectra before and after surface cleaning is shown in Figure 6. Doublets were fitted with a separation of 1.18 eV[66] and an area ratio of 1:2. Ultimately, before cleaning, the spectra were fit with three doublets, and after cleaning, were fit with two doublets. The species which was eliminated after cleaning (green shading) is attributed to sulphur-containing surface contamination[67], as seen in other sulphide materials[39]. The two strongest doublets (red dash & blue dot), separated by 0.3 eV are assigned to S^{2-} in CAS. Each doublet is attributed to one of the two different coordination sites, as described in the introduction, and shown in Figure 1. In the literature, little to no attempts at fitting the S 2p region have been made, and only one group fit it with more than one doublet[9,22], however, the signal-to-noise ratio (SNR) is poor and the authors state that the extra doublets are due to unreacted precursor. It is our opinion, however, that the extra sulphur peaks in that study were probably due to sputter damage, affirmed by the sputter profile shown there. The viability of the presence of two doublets in Figure 6 is initially confirmed by the poor quality of fit when using one doublet (see Figure S2), and is strengthened by: the area ratio between the doublets being 1:1, as expected from the crystal structure; that previously measured samples by the authors fit this way equally well[40]; and because of the large difference in coordination environments for the sulphur. Despite this, the specific assignment of the S 2p doublets to their corresponding coordination environment is unclear. Although the S1 environment is coordinated to an extra cation, two of the bonds with antimony are significantly longer (3.12 Å) than the others[37] (2.30 – 2.57 Å), and as such are believed to be governed by van der Waals forces[68]. Given this, the severely distorted structure of CAS, and the complications involved with predicting the binding energies of sulphur for complex systems[69], then the amount of charge transfer, differences in electronegativities of the cations, the effect of bond lengths and second-nearest neighbours all contribute differently to the binding energy, and as such, no definitive assignment is given here. Prior to cleaning, the sample showed no presence of sulphate species, as has been seen in previous reports of this material[27,40].

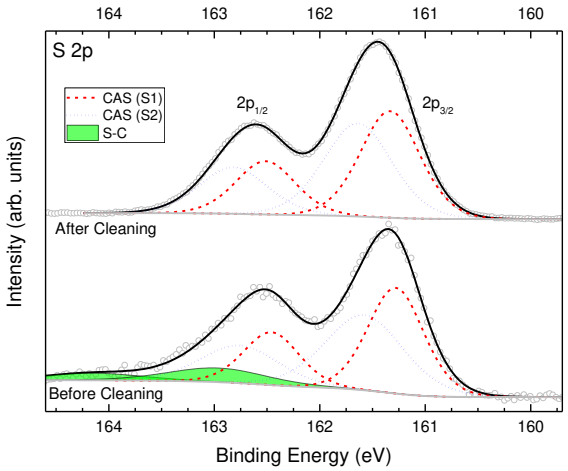

Figure 6: XPS spectra for the S 2p region of the CAS sample before and after surface cleaning. Peak envelope shown in black.

Generally, the binding energies reported in the literature for this material are in poor agreement with the values measured here. This is excepting one study with well fitted data[2], and other samples of this material measured by the authors[40]. However, it is believed that some studies are lacking a charge correction[21], or have misapplied one[28], but judging by the relative differences in binding energies between the peaks, these are also in agreement with the values measured here. Furthermore, other studies which are in contrast with our values suffer from the fact that the binding energies were either not quoted[27], not fitted in the case of multi-component regions[26], else the SNR were so poor that no values could be confidently assigned[25], and the merit of these analyses therefore cannot be evaluated. It is also noted that, as has been discussed above, the presence of contamination and oxide formation on materials can affect the measured binding energies, as well as the band positions which can also change as a function of composition and by the presence of mixed phases. In this respect, some studies seem to suffer from this without full acknowledgement of the ramifications[9,15,22].

As shown in Table 1, the shifts in binding energy before and after surface cleaning are rather small and therefore, it can be concluded that the surface cleaning employed here did not significantly affect the underlying material. Further discussion on the reported binding energies, including those from contamination, can be found in the SI, along with all fitted binding energies in Table S1. Also presented in the SI are the XPS-derived surface stoichiometry values, and a discussion and comparison of the effect of the thermal treatment stage of the growth with respect to the electronic structure and sample quality.

Table 1: XPS binding energies determined for the main peaks of CAS before and after surface cleaning with values for work function, ionisation potential and electron affinity also determined from XPS and optical absorption spectra. All values are given in eV and the peak FWHM are given in parentheses. Binding energies of all fitted peaks in this study can be found in Table S1.

Sample	$CuSbS_2$						
	Cu $2p_{3/2}$	Sb $3d_{5/2}$	S $2p_{3/2}$	S $2p_{3/2}$	WF	IP	EA
Before cleaning	931.97 (1.13)	529.11 (0.80)	161.28 (0.62)	161.58 (0.88)			
After cleaning	931.97 (1.13)	529.19 (0.86)	161.33 (0.66)	161.64 (0.76)	4.73	4.98	3.43

Band Edge Positions

When considering solar cell materials, another often overlooked point to consider is the position of the band edges and ultimately how this will affect the architecture of the cell. An oft quoted property of absorber materials is the band gap, and whilst a relevant band gap value is necessary for decent efficiencies, this can be largely compromised if the band alignments hinder charge carrier extraction.

Nevertheless, the direct and indirect band gaps of the $CuSbS_2$ sample were determined from the absorption spectra both at room and cryogenic temperatures[70,71], shown in the Tauc plots in Figure 7. Room temperature measurements (300 K) allow the extraction of both the direct (1.60 eV) and indirect (1.55 eV) band gaps, which are in agreement with a previous study, finding the direct transition to lie within 0.1 eV higher than the indirect transition, leading to previous misclassification of the fundamental gap of this material to be direct in nature[7]. The direct and indirect gaps at cryogenic temperatures (4 K) were also determined for comparison with the DFT calculations and were found to be 1.69 eV and 1.59 eV respectively. As the DFT HSE06 (0 K) direct and indirect band gaps were found to be 1.82 eV and 1.67 eV respectively, this is in satisfactory agreement with the experimental results at 4 K, with the slight discrepancy explained because of the lack of inclusion of excitonic effects which may affect the experimental absorption.

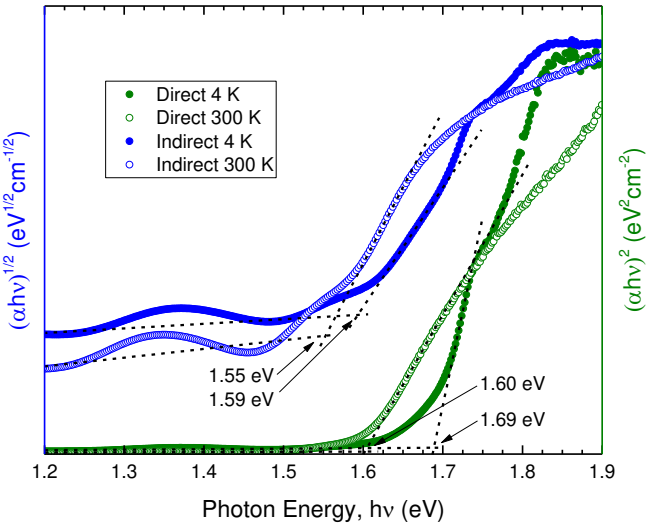

Figure 7: Optical absorption data from $CuSbS_2$. Tauc plot fittings for the direct and indirect gaps of the $CuSbS_2$ sample at 4 K and 300 K.

It is also important, at least from an initial cell-design perspective, that the relative energies between the conduction band minima (CBM) and valence band maxima (VBM) are known with respect to the vacuum level: these are the electron affinity (EA) and ionisation potential (IP) respectively. Direct measurements of IP are possible using XPS, the method of which is described elsewhere[39]. The IP and, as a consequence work function (WF), of the CAS sample after cleaning were determined to be 4.98 eV and 4.73 eV respectively from the fittings shown in Figure S8. By using a vacuum alignment procedure[72] and taking the measured indirect 300 K band gap value of 1.55 eV from Figure 7, this is shown graphically for comparison with CZTS, CIGS and CdS in Figure 8, with the values of IP and WF shown in Table 1. Consequently, the EA was calculated to be 3.43 eV by taking the difference between the measured IP and band gap, and is also shown in Table 1.

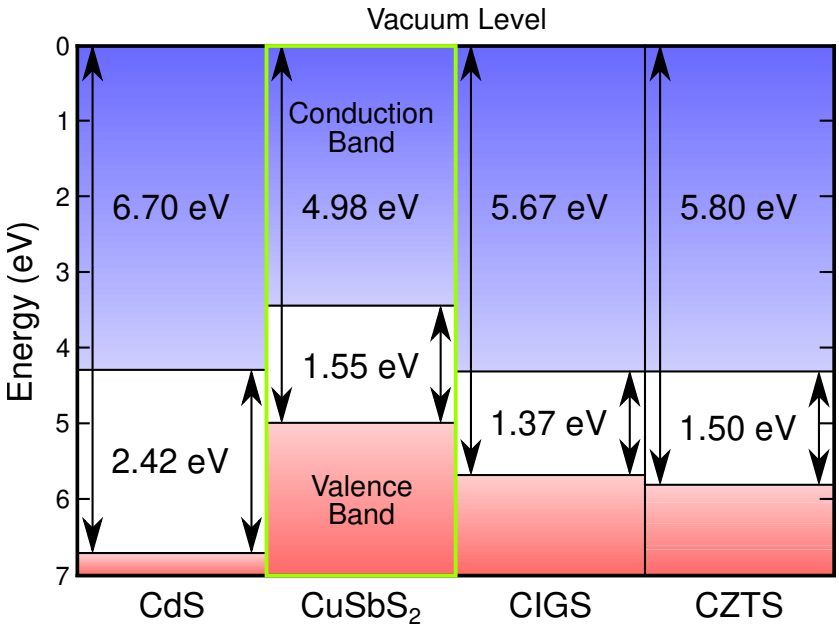

Figure 8: Vacuum-aligned band diagram for CAS from IP measurements using XPS and band gap from optical absorption and comparison with other common absorbers and the common n-type window layer material, CdS. Literature values of ionisation potential and band gap are taken for CdS[73], CIGS[74] and CZTS[73].

Although XPS can be used to great effect in determining band positions[75] and also performing band alignments at junction interfaces[76], it is not widely performed, especially on new materials. Hence these measurements are absent from the majority of the literature on CAS. However one study[15] using ultraviolet photoemission spectroscopy (UPS), measured a WF of 4.86 eV, in good agreement with our values, and an ionisation potential of 5.25 eV, which when taking into account the apparent level of contamination present in this cited study, is not unexpected as the fitting for the VBM is unclear. In another study, where there was extremely heavy antimony oxide contamination present, a very high IP was measured[40]. Coupled with the fact that a high band gap (2.75 eV) was measured in that particular study as well, this suggests that the presence of antimony oxide could be a contributing factor to the poor performance of CAS so far, because Sb_2O_3 has a relatively large band gap[77] and would act as an insulating layer within the cell. It is posited that only with the use of surface sensitive techniques such as XPS, that the true ramifications of this oxide formation can be determined, because as the oxide is very thin (<3nm, evidenced from the spectral ratios and estimated escape depth of electrons in Figure S6), optical measurements of the band gap would not be affected by it. Also, as the oxide crystallinity is probably poor and given the thinness of this layer, identification may be missed by XRD analysis. In this respect, surface sensitive XPS can provide indispensable information: identifying unwanted contaminants and also measuring the effect they have on the electronic structure.

It has been previously suggested that the poor open circuit voltage (V_{OC}) in CAS cells arises partly from a poor conduction band (CB) alignment with the n-type layer[4], and this is confirmed here in Figure 8, with the conduction band of CAS lying 0.85 eV higher than that of CdS, which with such a high conduction band offset (CBO), would suggest that a recombination centre would be present here[78]. In fact, in order to stop the formation of an electron barrier at the interface, the conduction band of the n-type layer should be 0–0.4 eV higher than that of the absorber[79], as is the case with both CIGS/CdS and CZTS/CdS as seen in Figure 8. It is therefore obvious that utilising traditional CIGS cell architectures for CAS is unfavourable for device performance. The use of CdS as the n-type layer not only creates the cliff-like CBO[4], but also undermines the goal of developing environmentally-friendly structures. It may also be the case that along with replacing the n-type layer, the back contact may also need

replacing as the work function of typically-used molybdenum may not be favourable for charge extraction. It is therefore apparent that further research is needed to identify more ideal partner materials for CAS in a cell[80], especially with regards to measuring band alignments in real systems.

Density of States

The IP found in the previous section is unusually low compared with other PV absorbers (see Figure 8). This has been seen previously in materials with non-bonding lone pairs[39], where this electronic structure feature was the reason for the remarkably high bands, causing a CB misalignment with CdS, and it is thought that a similar situation could be present in CAS as well. The partial density of states (pDoS) in the valence band along with the experimentally measured valence band spectra from XPS (after cleaning) are shown in Figure 9. A Shirley background was subtracted from the spectra to account for inelastically scattered electrons. The pDoS curves were corrected using standard photoionisation cross sections[81], convolved with a Gaussian function (0.38 eV FWHM) to account for thermal broadening and the spectrometer resolution, and then further convolved with a Lorentzian function (0.25 eV FWHM) to account for lifetime broadening. The corrected pDoS curves were then summed, and the total curve aligned to the XPS data for direct comparison. There is generally good agreement between the calculated density of states (DoS) and the XPS spectra, with all features accounted for and the relative intensities of the correct order. Especially, Cu 3d states of the main feature (II) and the leading edge at the top of the valence band (I) are reproduced well. The only differences arise at features III and IV (better shown in the zoomed region of Figure 9), probably due to final-state relaxation effects in XPS, which are known to shift features which are deeper in the valence band to lower binding energies[39,82].

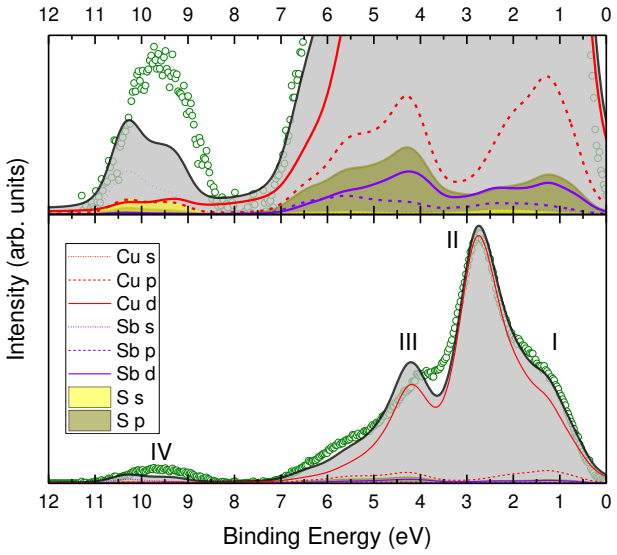

Figure 9: Simulated and measured VB spectra for CAS with respect to the Fermi level at 0 eV. Background subtracted XPS data is compared with broadened and corrected partial DoS curves. Top spectra shows intensity zoomed region to better show the underlying curves. Green data are from XPS and black curve with grey shading is the total summed DoS.

Following the excellent experimental corroboration from comparing XPS spectra and corrected DoS curves, it is now prudent to discuss the pDoS contributions with respect to the uncorrected curves due to the dominance of Cu 3d states arising from the large photoionisation cross section of this orbital. Thus, these are shown in Figure 10a, also with the corresponding DoS for the CB. Without the corrections, the VBDoS is still dominated by Cu 3d states, and the valence band shows three distinct features (V, VI & V*). Similarly to both CIGS and CZTS, the copper in CAS is tetrahedrally coordinated

to sulphur in the crystal structure and therefore the crystal field splits the Cu 3d orbitals into a non-bonding e doublet, and a t_2 triplet, which is able to bond[83]. These features are present in Figure 10 as the non-bonding e_g states (VI), and the bonding (V) and antibonding (V*) hybridisation of the t_{2g} states with S 3p states. The bottom of the highest valence band is comprised of bonding orbitals of S 3p states with a slight contribution from Sb 5p states (VII), and the antibonding states of this interaction form the main contribution to the conduction band (VII*).

Further insights into the bonding nature are gained when studying the states normally overwhelmed by intensity from Cu d/S p hybridisation and to this end, we consider the zoomed region of the valence and conduction band edges in Figure 10b. At first glance, it would seem that the Sb 5s states are localised at ~10 eV in feature VIII, which agrees with the classical model of lone pair electrons, that they are too tightly bound and therefore non-bonding. However, there are also Sb s states at the top of the valence band (X) and the bottom of the conduction band (X*), which suggests that the contribution here is due to interactions via the revised lone pair model[35]. In this model, the lone pair electrons firstly interact with S 3p electrons and the full antibonding orbital of this interaction is then sufficiently high so that it can subsequently interact with empty Sb 5p states, resulting in bonding states in the valence band (X) and antibonding states at the bottom of the conduction band (X*). Our findings, in agreement with previous analyses of the VBDoS of CAS[1,36], are in direct opposition to a more recent study which claimed that the Sb 5s lone pair is inert, localised and contributes nothing to bonding in the valence band[33]. We believe this interpretation to be incorrect for two main reasons: firstly, because the top of the valence band is so well reproduced between the DoS and XPS spectrum the underlying bonding nature is supported, even though the Sb states have weak cross sections when compared to the Cu states, and secondly, due to the distorted nature of the SbS_5 pyramids in the crystal structure, the revised lone pair model suggests that these interactions should indeed take place, and in fact stabilises the structure by projecting these states into the crystal void, whereas in undistorted structures, this interaction is symmetry forbidden[36].

The bonding mechanisms described above and the other main contributions are shown schematically in Figure 10c to more clearly demonstrate the proposed hybridisations from the configuration energies (CE), most importantly, the effect of the lone pairs, and the nature of the Cu 3d states in the valence band.

The described features are in agreement with previous analyses of CAS DoS calculations[1,7,33,36], however no solid link has been previously made to the effect of these features regarding the electronic properties. As discussed previously, much initial progress was made likening CAS to CIGS and also to CZTS, and the comparisons are still drawn in analyses of the DoS[36], especially regarding the Cu 3d/S 3p states in the valence band[7], which are indeed very similar to the tetrahedral environment also present in CIGS. However, the full merit of this practice is questioned when it is clear that the crystal structure of CAS is so different from CIGS, then so should be the DoS as the bonding is what leads to the adopted crystal structure. Clearly, from the CBDoS, Sb 5p states are the main cation contributor in CAS, whereas in CIGS, the bottom of the CB is mainly In/Ga s states[83–85]. Consequently, this has been recognised previously and found to be the reason why CAS shows superior absorption to CIGS[86], but no further discussions have been made[33]. We then posit that this difference is also the cause of the low IP found previously and discussed above. In CIGS, the In/Ga are in the 3+ oxidation state, as is Sb in CAS, however, being group III elements, In/Ga have formally empty valence s orbitals for the 3+ oxidation state ($[Kr]4d^{10}5s^{0}5p^{0}$/$[Ar]3d^{10}4s^{0}4p^{0}$), whereas in group V Sb, it is full ($[Kr]4d^{10}5s^{2}5p^{0}$). This means that in CIGS, empty cation s orbitals bond with full anion p orbitals to form regular full bonding states at the bottom of the valence band and empty antibonding states at the bottom of the conduction band, whereas in CAS the full Sb 5s orbital is available for bonding and due to the

mechanism described above, states are found throughout the valence band and at the bottom of the conduction band. It is unsurprising that the first conduction band of CAS is dominated by antibonding Sb 5p/S 3p states as Sb-5p are the first empty orbitals that are energetically within the proximity of the full S 3p orbitals. This is shown, in contrast to the empty states of CIGS, in the schematic configuration energy diagram in Figure 11, with the main contributions to the VBM and CBM marked. From this, we can also see that the empty cation s states in CIGS are energetically closer to the anion p orbital than the also empty cation p orbitals, and therefore the cation s nature of the CBM in CIGS is explained as well.

Although we believe that the Sb lone pair plays some effect in raising the energy levels of the bands in CAS, the Cu d states must also have an effect due to their dominating presence in the valence band. In other dominant d-orbital semiconductors, the chemical trend is that with increasing separation between the cation d and anion p levels, the VBM position rises, given a common-cation[87,88]. If one accept this, then by studying Figure 11, the CAS analogue replacing S with Se, that is $CuSbSe_2$ (CASe), should yield a lower IP even than CAS, and such has been reported previously[1,89]. This then, would suggest that CIGS, with common Cu-cation, and Se as an anion, should show a similar trend when compared to CAS. As this is not the case, it is then evident that it is the presence of antimony over indium/gallium which is responsible for the raising of the valence band, both through the addition of Sb 5s states to the valence band, but also the shifting of Cu 3d states within the VBM.

As has been shown before, the growth method can strongly affect the device quality with regards to contaminant formation. However, another issue is the formation of defects within the absorber material which can also affect device performance. 'Defect tolerance' is a term used when the formation of defects does not negatively affect the properties of a material and has been classified to occur when the VBM is antibonding in nature and the CBM is bonding in nature, so that defects would produce only shallow levels[90]. To this extent, CAS should benefit from at least some measure of this property because even though the CBM is predominantly antibonding Sb p/S p states, the VBM is strongly antibonding Cu d/S p with also a slight contribution from Sb s states due to the lone pair bonding mechanism. Furthermore, the dominant vacancy in CAS has been shown to be the acceptor copper vacancy (V_{Cu})[15] which leads to the inherent p-type conductivity and also the crystallographic differences between the two cation-anion environments makes CAS less prone to cation disorder, and the band tailing associated with it[3], both of which further support this idea that CAS should be defect tolerant.

These observations and reasoning all support the postulate that advancement in CAS research now requires a definitive move away from CIGS analogies. The lone pair of electrons from the antimony cation provides extra states to both the valence and conduction bands of CAS, which are not present in CIGS. This leads to a higher VBM level, resulting in a markedly low IP for CAS, which results in a performance-damaging CBO with CdS, which is commonly used in CIGS cells. Therefore, CAS should be developed, along with its true analogous materials (the [Cu-(Sb/Bi)-(S/Se)] family of systems), as its own class of earth-abundant absorber materials.

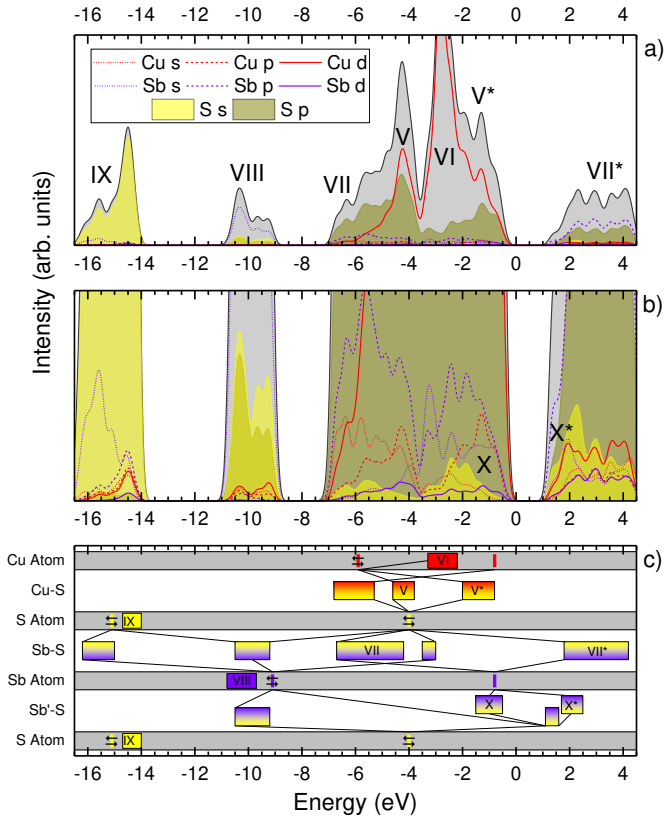

Figure 10: a) & b) Total and partial electronic density of states curves for CAS, with intensity zoomed region to more clearly show the underlying orbitals. Curves have been convolved with a Gaussian function (0.3 eV FWHM) in order to better distinguish features. DoS curves are aligned to the VBM. Black curve with grey shading is the total summed DoS. c) CEs for the valence orbitals[91,92] displayed with a schematic of the bonding hybridisations as discussed in the text. It is noted that the CE values do not take ionisation, multi-electron occupancy or hybridisation into account and are shown only as a schematic guide. Part labels are discussed and referred to throughout the text.

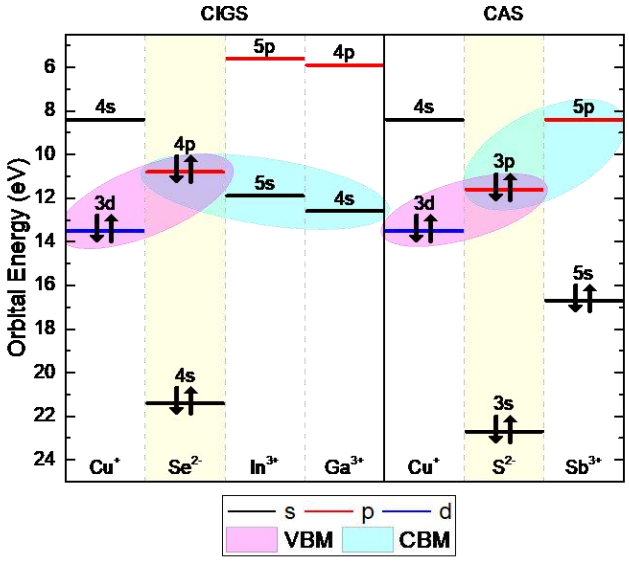

Figure 11: CEs[91,92] for the valence orbitals of CIGS and CAS. The formal ionic occupancy of the orbitals within the materials are marked and the main orbital contributions to the VBM and CBM are shown.

Conclusions

The valence band density of states and the size and nature of the band gaps of the promising absorber material, $CuSbS_2$ have been compared experimentally and theoretically for the first time. We show that the strong Cu d nature of the valence band obscures states arising from the second cation, antimony, but which play a role in determining the properties of the material. In contrast with CIGS, the conduction band minima consists of second-cation p/anion p states rather than second-cation s/anion p states as in CIGS; a result of Sb^{3+} being a group V element rather than the group III $(In/Ga)^{3+}$ in CIGS. The full Sb 5s states therefore also feature at the top of the valence band through the revised lone pair model, along with Sb 5p states. These extra contributions to the valence band play some role in raising the VBM and causing the low IP of 4.98 eV observed here. The band levels measured here support the reasoning that CdS is an inappropriate n-type window layer for CAS because of the large CBO, resulting from the low EA (3.43 eV) which was determined using a combination of IP measurements from XPS and a band gap measurement of 1.55 eV from the room temperature indirect absorption spectra. This approach to cell design, which arises from CIGS development, is part of the reason that CAS has seen poor performance. We have also shown a thorough core-level XPS analysis of CAS, which reveals that the two sulphur coordination environments can be determined by XPS, and also the effect that contamination can have, which is crucial given the complexities of the spectra of this material. Following a thorough literature survey of this material, it is believed that these complexities have led to misinterpretations of the spectra, and therefore this could have contributed to the poor performance of CAS so far as well. It is therefore clear that the use of CdS as the n-type layer in CAS cells is less favourable than for CIGS cells. However, with alternative n-type material with better band alignments, the potential of CAS as a solar absorber remains.

Acknowledgements

This work was supported by the UK Engineering and Physical Sciences Research Council (EPSRC). TJW & MB acknowledge funding through EPSRC studentships (Grant No. EP/J50047/1, EP/K503095/1, & EP/L505018/1). The synthesis of the samples was supported by U. S. Department of Energy, Office of Energy Efficiency and Renewable Energy, under Contract No. DE-AC36-08GO28308 to National Renewable Energy Laboratory. The computational work in this article made use of the ARCHER U.K. National Supercomputing Service (http://www.archer.ac.uk), via our membership of the U.K.'s HEC Materials Chemistry Consortium, which is funded by EPSRC (Grant No. EP/L000202), and the UCL Legion (Legion@UCL) and Grace (Grace@UCL) HPC Facilities. DOS and TDV acknowledge funding through EPSRC (Grant No. EP/N01572X/1 & EP/N015800/1) and membership of the Materials Design Network. CNS is grateful to EPSRC and the Department of Chemistry at UCL for the provision of a Doctoral Training Partnership studentship (Ref. No. 1492829).

References

(1) Temple, D. J.; Kehoe, A. B.; Allen, J. P.; Watson, G. W.; Scanlon, D. O. Geometry, Electronic Structure, and Bonding in CuMCh 2 (M = Sb, Bi; Ch = S, Se): Alternative Solar Cell Absorber Materials? *J. Phys. Chem. C* **2012**, *116* (13), 7334–7340.

(2) Wan, L.; Ma, C.; Hu, K.; Zhou, R.; Mao, X.; Pan, S.; Wong, L. H.; Xu, J. Two-Stage Co-Evaporated CuSbS2 Thin Films for Solar Cells. *J. Alloys Compd.* **2016**, *680*, 182–190.

(3) de Souza Lucas, F. W.; Welch, A. W.; Baranowski, L. L.; Dippo, P. C.; Hempel, H.; Unold, T.; Eichberger, R.; Blank, B.; Rau, U.; Mascaro, L. H.; Zakutayev, A. Effects of Thermochemical Treatment on CuSbS 2 Photovoltaic Absorber Quality and Solar Cell Reproducibility. *J. Phys. Chem. C* **2016**, *120* (33), 18377–18385.

(4) Welch, A. W.; Baranowski, L. L.; Zawadzki, P.; DeHart, C.; Johnston, S.; Lany, S.; Wolden, C. A.;

Zakutayev, A. Accelerated Development of CuSbS 2 Thin Film Photovoltaic Device Prototypes. *Prog. Photovoltaics Res. Appl.* **2016**, *24* (7), 929–939.

(5) Rodríguez-Lazcano, Y.; Nair, M. T. S.; Nair, P. K. CuSbS2 Thin Film Formed through Annealing Chemically Deposited Sb2S3–CuS Thin Films. *J. Cryst. Growth* **2001**, *223* (3), 399–406.

(6) Kehoe, A. B.; Temple, D. J.; Watson, G. W.; Scanlon, D. O. Cu3MCh3 (M = Sb, Bi; Ch = S, Se) as Candidate Solar Cell Absorbers: Insights from Theory. *Phys. Chem. Chem. Phys.* **2013**, *15* (37), 15477.

(7) Kumar, M.; Persson, C. CuSbS2 and CuBiS2 as Potential Absorber Materials for Thin-Film Solar Cells. *J. Renew. Sustain. Energy* **2013**, *5* (3), 31616.

(8) Ganose, A. M.; Savory, C. N.; Scanlon, D. O. Beyond Methylammonium Lead Iodide: Prospects for the Emergent Field of Ns 2 Containing Solar Absorbers. *Chem. Commun.* **2017**, *53* (1), 20–44.

(9) Ornelas-Acosta, R. E.; Shaji, S.; Avellaneda, D.; Castillo, G. a.; Das Roy, T. K.; Krishnan, B. Thin Films of Copper Antimony Sulfide: A Photovoltaic Absorber Material. *Mater. Res. Bull.* **2015**, *61*, 215–225.

(10) Hofmann, W. Strukturelle Und Morphologische Zusammenhänge Bei Erzen Vom Formeltyp ABC2. *Zeitschrift für Krist. - Cryst. Mater.* **1933**, *84* (1–6), 177–203.

(11) Rodríguez-Lazcano, Y.; Nair, M. T. S.; Nair, P. K. Photovoltaic P-I-N Structure of Sb2S3 and CuSbS2 Absorber Films Obtained via Chemical Bath Deposition. *J. Electrochem. Soc.* **2005**, *152* (8), G635–G638.

(12) Garza, C.; Shaji, S.; Arato, A.; Perez Tijerina, E.; Alan Castillo, G.; Das Roy, T. K.; Krishnan, B. P-Type CuSbS2 Thin Films by Thermal Diffusion of Copper into Sb2S3. *Sol. Energy Mater. Sol. Cells* **2011**, *95* (8), 2001–2005.

(13) Septina, W.; Ikeda, S.; Iga, Y.; Harada, T.; Matsumura, M. Thin Film Solar Cell Based on CuSbS2 Absorber Fabricated from an Electrochemically Deposited Metal Stack. *Thin Solid Films* **2014**, *550*, 700–704.

(14) Popovici, I.; Duta, A. Tailoring the Composition and Properties of Sprayed CuSbS 2 Thin Films by Using Polymeric Additives. *Int. J. Photoenergy* **2012**, *2012*, 1–6.

(15) Yang, B.; Wang, L.; Han, J.; Zhou, Y.; Song, H.; Chen, S.; Zhong, J.; Lv, L.; Niu, D.; Tang, J. CuSbS 2 as a Promising Earth-Abundant Photovoltaic Absorber Material: A Combined Theoretical and Experimental Study. *Chem. Mater.* **2014**, *26* (10), 3135–3143.

(16) Colombara, D.; Peter, L. M.; Rogers, K. D.; Painter, J. D.; Roncallo, S. Formation of CuSbS2 and CuSbSe2 Thin Films via Chalcogenisation of Sb–Cu Metal Precursors. *Thin Solid Films* **2011**, *519* (21), 7438–7443.

(17) Krishnan, B.; Shaji, S.; Ernesto Ornelas, R. Progress in Development of Copper Antimony Sulfide Thin Films as an Alternative Material for Solar Energy Harvesting. *J. Mater. Sci. Mater. Electron.* **2015**, *26* (7), 4770–4781.

(18) Rabhi, A.; Kanzari, M.; Rezig, B. Optical and Structural Properties of CuSbS2 Thin Films Grown by Thermal Evaporation Method. *Thin Solid Films* **2009**, *517* (7), 2477–2480.

(19) Welch, A. W.; Zawadzki, P. P.; Lany, S.; Wolden, C. A.; Zakutayev, A. Self-Regulated Growth and Tunable Properties of CuSbS2 Solar Absorbers. *Sol. Energy Mater. Sol. Cells* **2015**, *132*, 499–506.

(20) Manolache, S.; Duta, A.; Isac, L.; Nanu, M.; Goossens, A.; Schoonman, J. The Influence of the Precursor Concentration on CuSbS2 Thin Films Deposited from Aqueous Solutions. *Thin Solid Films* **2007**, *515* (15), 5957–5960.

(21) Ramos Aquino, J. A.; Rodriguez Vela, D. L.; Shaji, S.; Avellaneda, D. A.; Krishnan, B. Spray Pyrolysed Thin Films of Copper Antimony Sulfide as Photovoltaic Absorber. *Phys. status solidi* **2016**, *13* (1), 24–29.

(22) Ornelas-Acosta, R. E.; Avellaneda, D.; Shaji, S.; Castillo, G. a.; Das Roy, T. K.; Krishnan, B. CuSbS2 Thin Films by Heating Sb2S3/Cu Layers for PV Applications. *J. Mater. Sci. Mater. Electron.* **2014**, *25* (10), 4356–4362.

(23) Rastogi, A. C.; Janardhana, N. R. Properties of CuSbS2 Thin Films Electrodeposited from Ionic Liquids as P-Type Absorber for Photovoltaic Solar Cells. *Thin Solid Films* **2014**, *565*, 285–292.

(24) Suehiro, S.; Horita, K.; Yuasa, M.; Tanaka, T.; Fujita, K.; Ishiwata, Y.; Shimanoe, K.; Kida, T. Synthesis of Copper–Antimony-Sulfide Nanocrystals for Solution-Processed Solar Cells. *Inorg. Chem.* **2015**, *54* (16), 7840–7845.

(25) An, C.; Liu, Q.; Tang, K.; Yang, Q.; Chen, X.; Liu, J.; Qian, Y. The Influences of Surfactant Concentration on the Quality of Chalcostibite Nanorods. *J. Cryst. Growth* **2003**, *256* (1–2), 128–133.

(26) Suriakarthick, R.; Nirmal Kumar, V.; Shyju, T. S.; Gopalakrishnan, R. Effect of Substrate Temperature on Copper Antimony Sulphide Thin Films from Thermal Evaporation. *J. Alloys Compd.* **2015**, *651*, 423–433.

(27) Su, H.; Xie, Y.; Wan, S.; Li, B.; Qian, Y. A Novel One-Step Solvothermal Route to Nanocrystalline CuSbS2 and Ag3SbS3. *Solid State Ionics* **1999**, *123* (1–4), 319–324.

(28) Ramasamy, K.; Gupta, R. K.; Sims, H.; Palchoudhury, S.; Ivanov, S.; Gupta, A. Layered Ternary Sulfide CuSbS 2 Nanoplates for Flexible Solid-State Supercapacitors. *J. Mater. Chem. A* **2015**, *3* (25), 13263–13274.

(29) Ramasamy, K.; Tien, B.; Archana, P. S.; Gupta, A. Copper Antimony Sulfide (CuSbS2) Mesocrystals: A Potential Counter Electrode Material for Dye-Sensitized Solar Cells. *Mater. Lett.* **2014**, *124*, 227–230.

(30) Choi, Y. C.; Yeom, E. J.; Ahn, T. K.; Seok, S. Il. CuSbS 2 -Sensitized Inorganic-Organic Heterojunction Solar Cells Fabricated Using a Metal-Thiourea Complex Solution. *Angew. Chemie Int. Ed.* **2015**, *54* (13), 4005–4009.

(31) Marino, C.; Block, T.; Pöttgen, R.; Villevieille, C. CuSbS2 as a Negative Electrode Material for Sodium Ion Batteries. *J. Power Sources* **2017**, *342*, 616–622.

(32) Banu, S.; Ahn, S. J.; Ahn, S. K.; Yoon, K.; Cho, A. Fabrication and Characterization of Cost-Efficient CuSbS2 Thin Film Solar Cells Using Hybrid Inks. *Sol. Energy Mater. Sol. Cells* **2016**, *151*, 14–23.

(33) Maeda, T.; Wada, T. First-Principles Study of Electronic Structure of CuSbS2 and CuSbSe2 Photovoltaic Semiconductors. *Thin Solid Films* **2015**, *582*, 401–407.

(34) Makovicky, E. Crystal Structures of Sulfides and Other Chalcogenides. *Rev. Mineral. Geochemistry* **2006**, *61* (1), 7–125.

(35) Walsh, A.; Payne, D. J.; Egdell, R. G.; Watson, G. W. Stereochemistry of Post-Transition Metal Oxides: Revision of the Classical Lone Pair Model. *Chem. Soc. Rev.* **2011**, *40* (9), 4455–4463.

(36) Dufton, J. T. R.; Walsh, A.; Panchmatia, P. M.; Peter, L. M.; Colombara, D.; Islam, M. S. Structural and Electronic Properties of CuSbS2 and CuBiS2: Potential Absorber Materials for Thin-Film Solar Cells. *Phys. Chem. Chem. Phys.* **2012**, *14* (20), 7229.

(37) Kyono, A. Crystal Structures of Chalcostibite (CuSbS2) and Emplectite (CuBiS2): Structural Relationship of Stereochemical Activity between Chalcostibite and Emplectite. *Am. Mineral.* **2005**, *90* (1), 162–165.

(38) Birkett, M.; Savory, C. N.; Fioretti, A. N.; Thompson, P.; Muryn, C. A.; Weerakkody, A. D.; Mitrovic, I. Z.; Hall, S.; Treharne, R.; Dhanak, V. R.; Scanlon, D. O.; Zakutayev, A.; Veal, T. D. Atypically Small Temperature-Dependence of the Direct Band Gap in the Metastable Semiconductor Copper Nitride <math> <mrow> <msub> <mi>Cu</mi> <mn>3</mn> </msub> <mi mathvariant="normal">N</mi> </mrow> </math>. *Phys. Rev. B* **2017**, *95* (11), 115201.

(39) Whittles, T. J.; Burton, L. A.; Skelton, J. M.; Walsh, A.; Veal, T. D.; Dhanak, V. R. Band Alignments, Valence Bands, and Core Levels in the Tin Sulfides SnS, SnS 2 , and Sn 2 S 3 : Experiment and Theory. *Chem. Mater.* **2016**, *28* (11), 3718–3726.

(40) Peccerillo, E.; Major, J.; Phillips, L.; Treharne, R.; Whittles, T. J.; Dhanak, V.; Halliday, D.; Durose, K. Characterization of Sulfurized CuSbS2 Thin Films for PV Applications. In *2014 IEEE 40th Photovoltaic Specialist Conference (PVSC)*; IEEE, 2014; pp 0266–0269.

(41) Zhong, J.; Xiang, W.; Cai, Q.; Liang, X. Synthesis, Characterization and Optical Properties of Flower-like Cu3BiS3 Nanorods. *Mater. Lett.* **2012**, *70*, 63–66.

(42) Kresse, G.; Hafner, J. Ab Initio Molecular Dynamics for Liquid Metals. *Phys. Rev. B* **1993**, *47* (1), 558–561.

(43) Kresse, G.; Hafner, J. Ab Initio Molecular-Dynamics Simulation of the Liquid-Metal–amorphous-Semiconductor Transition in Germanium. *Phys. Rev. B* **1994**, *49* (20), 14251–14269.

(44) Kresse, G.; Furthm?ller, J. Efficiency of Ab-Initio Total Energy Calculations for Metals and Semiconductors Using a Plane-Wave Basis Set. *Comput. Mater. Sci.* **1996**, *6* (1), 15–50.

(45) Kresse, G.; Furthmüller, J. Efficient Iterative Schemes for Ab Initio Total-Energy Calculations Using a Plane-Wave Basis Set. *Phys. Rev. B* **1996**, *54* (16), 11169–11186.

(46) Krukau, A. V.; Vydrov, O. a.; Izmaylov, A. F.; Scuseria, G. E. Influence of the Exchange Screening Parameter on the Performance of Screened Hybrid Functionals. *J. Chem. Phys.* **2006**, *125* (22), 224106.

(47) Perdew, J. P.; Burke, K.; Ernzerhof, M. Generalized Gradient Approximation Made Simple. *Phys. Rev. Lett.* **1996**, *77* (18), 3865–3868.

(48) Yang, R. X.; Butler, K. T.; Walsh, A. Assessment of Hybrid Organic–Inorganic Antimony Sulfides for Earth-Abundant Photovoltaic Applications. *J. Phys. Chem. Lett.* **2015**, *6* (24), 5009–5014.

(49) Blöchl, P. E. Projector Augmented-Wave Method. *Phys. Rev. B* **1994**, *50* (24), 17953–17979.

(50) Rath, T.; MacLachlan, A. J.; Brown, M. D.; Haque, S. A. Structural, Optical and Charge Generation Properties of Chalcostibite and Tetrahedrite Copper Antimony Sulfide Thin Films Prepared from Metal Xanthates. *J. Mater. Chem. A* **2015**, *3* (47), 24155–24162.

(51) Efthimiopoulos, I.; Buchan, C.; Wang, Y. Structural Properties of Sb2S3 under Pressure: Evidence of an Electronic Topological Transition. *Sci. Rep.* **2016**, *6* (April), 24246.

(52) Pronti, L.; Felici, A. C.; Alesiani, M.; Tarquini, O.; Bracciale, M. P.; Santarelli, M. L.; Pardini, G.; Piacentini, M. Characterisation of Corrosion Layers Formed under Burial Environment of

Copper-Based Greek and Roman Coins from Pompeii. *Appl. Phys. A* **2015**, *121* (1), 59–68.

(53) Mernagh, T. P.; Trudu, A. G. A Laser Raman Microprobe Study of Some Geologically Important Sulphide Minerals. *Chem. Geol.* **1993**, *103* (1–4), 113–127.

(54) Qiu, X. D.; Ji, S. L.; Chen, C.; Liu, G. Q.; Ye, C. H. Synthesis, Characterization, and Surface-Enhanced Raman Scattering of near Infrared Absorbing Cu3SbS3 Nanocrystals. *Crystengcomm* **2013**, *15* (48), 10431.

(55) Aup-Ngoen, K.; Thongtem, T.; Thongtem, S. Characterization of Cu3SbS4 Microflowers Produced by a Cyclic Microwave Radiation. *Mater. Lett.* **2012**, *66* (1), 182–186.

(56) Mesa, F.; Chamorro, W.; Vallejo, W.; Baier, R.; Dittrich, T.; Grimm, A.; Lux-Steiner, M. C.; Sadewasser, S. Junction Formation of Cu 3 BiS 3 Investigated by Kelvin Probe Force Microscopy and Surface Photovoltage Measurements. *Beilstein J. Nanotechnol.* **2012**, *3* (1), 277–284.

(57) Lebugle, A.; Axelsson, U.; Nyholm, R.; Mårtensson, N. Experimental L and M Core Level Binding Energies for the Metals 22 Ti to 30 Zn. *Phys. Scr.* **1981**, *23* (5A), 825–827.

(58) Coster, D.; L. Kronig, R. De. New Type of Auger Effect and Its Influence on the X-Ray Spectrum. *Physica* **1935**, *2* (1–12), 13–24.

(59) Nyholm, R.; Martensson, N.; Lebugle, A.; Axelsson, U. Auger and Coster-Kronig Broadening Effects in the 2p and 3p Photoelectron Spectra from the Metals 22 Ti- 30 Zn. *J. Phys. F Met. Phys.* **1981**, *11* (8), 1727–1733.

(60) Delobel, R.; Baussart, H.; Leroy, J.-M.; Grimblot, J.; Gengembre, L. X-Ray Photoelectron Spectroscopy Study of Uranium and Antimony Mixed Metal-Oxide Catalysts. *J. Chem. Soc. Faraday Trans. 1 Phys. Chem. Condens. Phases* **1983**, *79* (4), 879.

(61) Morgan, W. E.; Stec, W. J.; van Wazer, J. R. Inner-Orbital Binding Energy Shifts of Antimony and Bismuth Compounds. *Inorg. Chem.* **1972**, *12* (4), 953–955.

(62) Garbassi, F. XPS and AES Study of Antimony Oxides. *Surf. Interface Anal.* **1980**, *2* (5), 165–169.

(63) Tang, X.; Welzenis, R. G. van; Setten, F. M. van; Bosch, A. J. Oxidation of the InSb Surface at Room Temperature. *Semicond. Sci. Technol.* **1986**, *1* (6), 355–365.

(64) Petit, E. J.; Riga, J.; Caudano, R. Surface and Interface XPS Characterization of the Oxide Layer Grown on Antimony under UV Laser Irradiation. *Surf. Sci.* **1991**, *251–252*, 529–534.

(65) Payne, B. P.; Biesinger, M. C.; McIntyre, N. S. X-Ray Photoelectron Spectroscopy Studies of Reactions on Chromium Metal and Chromium Oxide Surfaces. *J. Electron Spectros. Relat. Phenomena* **2011**, *184* (1–2), 29–37.

(66) Barrie, A.; Drummond, I. W.; Herd, Q. C. Correlation of Calculated and Measured 2p Spin-Orbit Splitting by Electron Spectroscopy Using Monochromatic X-Radiation. *J. Electron Spectros. Relat. Phenomena* **1974**, *5* (1), 217–225.

(67) Lindberg, B. J.; Hamrin, K.; Johansson, G.; Gelius, U.; Fahlman, A.; Nordling, C.; Siegbahn, K. Molecular Spectroscopy by Means of ESCA II. Sulfur Compounds. Correlation of Electron Binding Energy with Structure. *Phys. Scr.* **1970**, *1* (5–6), 286–298.

(68) Ramasamy, K.; Sims, H.; Butler, W. H.; Gupta, A. Selective Nanocrystal Synthesis and Calculated Electronic Structure of All Four Phases of Copper–Antimony–Sulfide. *Chem. Mater.* **2014**, *26* (9), 2891–2899.

(69) Gerson, A. R.; Bredow, T. Interpretation of Sulphur 2p XPS Spectra in Sulfide Minerals by Means

of Ab Initio Calculations. *Surf. Interface Anal.* **2000**, *29* (2), 145–150.

(70) Viezbicke, B. D.; Patel, S.; Davis, B. E.; Birnie, D. P. Evaluation of the Tauc Method for Optical Absorption Edge Determination: ZnO Thin Films as a Model System. *Phys. status solidi* **2015**, *252* (8), 1700–1710.

(71) Tauc, J.; Grigorovici, R.; Vancu, A. Optical Properties and Electronic Structure of Amorphous Germanium. *Phys. status solidi* **1966**, *15* (2), 627–637.

(72) Klein, A. Energy Band Alignment in Chalcogenide Thin Film Solar Cells from Photoelectron Spectroscopy. *J. Phys. Condens. Matter* **2015**, *27* (13), 134201.

(73) Burton, L. A.; Walsh, A. Band Alignment in SnS Thin-Film Solar Cells: Possible Origin of the Low Conversion Efficiency. *Appl. Phys. Lett.* **2013**, *102* (13), 132111.

(74) Hinuma, Y.; Oba, F.; Kumagai, Y.; Tanaka, I. Ionization Potentials of (112) and (112¯) Facet Surfaces of CuInSe2 and CuGaSe2. *Phys. Rev. B* **2012**, *86* (24), 245433.

(75) Burton, L. A.; Whittles, T. J.; Hesp, D.; Linhart, W. M.; Skelton, J. M.; Hou, B.; Webster, R. F.; O'Dowd, G.; Reece, C.; Cherns, D.; Fermin, D. J.; Veal, T. D.; Dhanak, V. R.; Walsh, A. Electronic and Optical Properties of Single Crystal SnS 2 : An Earth-Abundant Disulfide Photocatalyst. *J. Mater. Chem. A* **2016**, *4* (4), 1312–1318.

(76) Durose, K.; Asher, S. E.; Jaegermann, W.; Levi, D.; McCandless, B. E.; Metzger, W.; Moutinho, H.; Paulson, P. D.; Perkins, C. L.; Sites, J. R.; Teeter, G.; Terheggen, M. Physical Characterization of Thin-Film Solar Cells. *Prog. Photovoltaics* **2004**, *12* (2–3), 177–217.

(77) Allen, J. P.; Carey, J. J.; Walsh, A.; Scanlon, D. O.; Watson, G. W. Electronic Structures of Antimony Oxides. *J. Phys. Chem. C* **2013**, *117* (28), 14759–14769.

(78) Sinsermsuksakul, P.; Hartman, K.; Bok Kim, S.; Heo, J.; Sun, L.; Hejin Park, H.; Chakraborty, R.; Buonassisi, T.; Gordon, R. G. Enhancing the Efficiency of SnS Solar Cells via Band-Offset Engineering with a Zinc Oxysulfide Buffer Layer. *Appl. Phys. Lett.* **2013**, *102* (5), 53901.

(79) Minemoto, T.; Matsui, T.; Takakura, H.; Hamakawa, Y.; Negami, T.; Hashimoto, Y.; Uenoyama, T.; Kitagawa, M. Theoretical Analysis of the Effect of Conduction Band Offset of window/CIS Layers on Performance of CIS Solar Cells Using Device Simulation. *Sol. Energy Mater. Sol. Cells* **2001**, *67* (1–4), 83–88.

(80) Baranowski, L. L.; Christensen, S.; Welch, A. W.; Lany, S.; Young, M.; Toberer, E. S.; Zakutayev, A. Conduction Band Position Tuning and Ga-Doping in (Cd,Zn)S Alloy Thin Films. *Mater. Chem. Front.* **2017**.

(81) Yeh, J. J.; Lindau, I. Atomic Subshell Photoionization Cross Sections and Asymmetry Parameters: $1 \leqslant Z \leqslant 103$. *At. Data Nucl. Data Tables* **1985**, *32* (1), 1–155.

(82) Ley, L.; Pollak, R. a.; McFeely, F. R.; Kowalczyk, S. P.; Shirley, D. a. Total Valence-Band Densities of States of III-V and II-VI Compounds from X-Ray Photoemission Spectroscopy. *Phys. Rev. B* **1974**, *9* (2), 600–621.

(83) Zhang, Y.; Yuan, X.; Sun, X.; Shih, B.-C.; Zhang, P.; Zhang, W. Comparative Study of Structural and Electronic Properties of Cu-Based Multinary Semiconductors. *Phys. Rev. B* **2011**, *84* (7), 75127.

(84) Maeda, T.; Wada, T. Characteristics of Chemical Bond and Vacancy Formation in Chalcopyrite-Type CuInSe 2 and Related Compounds. *Phys. status solidi* **2009**, *6* (5), 1312–1316.

(85) Chen, X.-D.; Chen, L.; Sun, Q.-Q.; Zhou, P.; Zhang, D. W. Hybrid Density Functional Theory Study

of Cu(In1−xGax)Se2 Band Structure for Solar Cell Application. *AIP Adv.* **2014**, *4* (8), 87118.

(86) Yu, L.; Kokenyesi, R. S.; Keszler, D. A.; Zunger, A. Inverse Design of High Absorption Thin-Film Photovoltaic Materials. *Adv. Energy Mater.* **2013**, *3* (1), 43–48.

(87) Wei, S. H.; Zunger, A. Calculated Natural Band Offsets of All II-VI and III-V Semiconductors: Chemical Trends and the Role of Cation D Orbitals. *Appl. Phys. Lett.* **1998**, *72* (16), 2011–2013.

(88) Wei, S.-H.; Zunger, A. Role of Metal D States in II-VI Semiconductors. *Phys. Rev. B* **1988**, *37* (15), 8958–8981.

(89) Xue, D.-J.; Yang, B.; Yuan, Z.-K.; Wang, G.; Liu, X.; Zhou, Y.; Hu, L.; Pan, D.; Chen, S.; Tang, J. CuSbSe 2 as a Potential Photovoltaic Absorber Material: Studies from Theory to Experiment. *Adv. Energy Mater.* **2015**, *5* (23), 1501203.

(90) Zakutayev, A.; Caskey, C. M.; Fioretti, A. N.; Ginley, D. S.; Vidal, J.; Stevanovic, V.; Tea, E.; Lany, S. Defect Tolerant Semiconductors for Solar Energy Conversion. *J. Phys. Chem. Lett.* **2014**, *5* (7), 1117–1125.

(91) Mann, J. B.; Meek, T. L.; Allen, L. C. Configuration Energies of the Main Group Elements. *J. Am. Chem. Soc.* **2000**, *122* (12), 2780–2783.

(92) Mann, J. B.; Meek, T. L.; Knight, E. T.; Capitani, J. F.; Allen, L. C. Configuration Energies of the D-Block Elements. *J. Am. Chem. Soc.* **2000**, *122* (21), 5132–5137.

- PV
- CIGS
- CdTe
- CAS
- CZTS
- XPS
- FTIR
- UHV
- SEC
- VB
- BE
- XRD
- SNR
- FWHM
- CBM
- VBM
- EA
- IP
- WF
- UPS
- V_{OC}
- CB
- CBO
- pDoS
- DoS
- CE

- CASe
- V_{Cu}
- DFT
- VASP
- GGA